Title

A Theoretical and Experimental Investigation of the Reduction of Dinuclear Persulfide-Bridged Ruthenium Complexes

Journal

Inorganic Chemistry

ISSN

0020-1669

Authors

Lotlikar, Piyusha S

Wilson, Justin J

Publication Date

2026-09-01

DOI

10.1021/acs.inorgchem.6c02292

A Theoretical and Experimental Investigation of the Reduction of Dinuclear Persulfide-Bridged Ruthenium Complexes

Piyusha S. Lotlikar[1,2] and Justin J. Wilson[1,2]*

[1]Department of Chemistry and Chemical Biology, Cornell University, Ithaca, New York 14853, United States

[2]Department of Chemistry and Biochemistry, University of California, Santa Barbara, California 93106, United States

*justinjwilson@ucsb.edu

Abstract

Previously, the dinuclear persulfide-bridged ruthenium complex $[(H_2O)(NH_3)_4Ru(\mu\text{-}S_2)Ru(NH_3)_4(OH_2)]^{4+}$ was demonstrated to be a reduction-activated H_2S donor, acting as a promising complex for the biological delivery of this gasotransmitter. Building on previous studies, other complexes bearing the [RuSSRu] motif were investigated for H_2S release. In this study, a previously reported persulfide-bridged complex $[(acac)(Me_3TACN)Ru(\mu\text{-}S_2)Ru(Me_3TACN)(acac)]^{2+}$ was evaluated. The crystal structure of a new crystal form of this complex was determined revealing a new orientation of supporting ligands about the *trans*-[RuSSRu] motif. Furthermore, resonance Raman spectroscopy revealed symmetric Ru–S and S–S stretching frequencies of 418 and 528 cm^{-1}, respectively. Lastly, the electrochemistry of this complex was probed in aqueous

buffer revealing an irreversible reduction at –758 mV vs SCE. The reactivity of [(acac)(Me_3TACN)Ru(μ-S_2)Ru(Me_3TACN)(acac)]$^{2+}$ was studied in the presence of different biological reductants and unexpectedly remained intact, showing no evidence for S–S bond cleavage or release of H_2S. To investigate the difference between this complex and [(H_2O)(NH_3)$_4$Ru(μ-S_2)Ru(NH_3)$_4$(OH_2)]$^{4+}$, density functional theory (DFT) calculations were performed, which revealed that [(acac)(Me_3TACN)Ru(μ-S_2)Ru(Me_3TACN)(acac)]$^{2+}$ possesses unoccupied ligand-based π* orbitals that more readily accept electrons than S–S bond destabilizing σ* orbitals. These computational findings validate our experimental results and provide guiding principles required for future compound design.

Introduction

Hypoxia, a common phenotype in human disease, is defined as depleted levels of oxygen in bodily tissues. It is a characteristic feature of many conditions such as cancer, respiratory disorders, and cardiovascular disease, among others.[1–7] The ubiquity of hypoxia in human pathologies has made it a common target for the development of drug candidates.[1,8,9] For example, the oxygen-deficient environment of hypoxic tissues can be leveraged to design hypoxia-selective prodrugs, which are activated by chemical reduction.[10–12] Redox-active organic compounds, particularly *N*-oxides and nitroimidazoles, have been extensively studied for this application.[12–17] Coordination complexes are also promising candidates as hypoxia-activated prodrugs.[18,19] Altering the ligand types within these complexes can lead to predictable well-defined changes in redox potential, while also optimizing other important biological properties, like lipophilicity and stability.

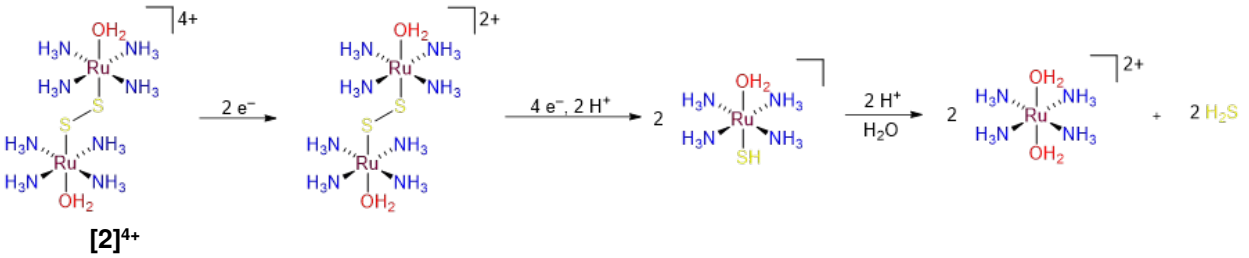

Scheme 1. Schematic representation of the 4e⁻ reduction of **[2]**$^{4+}$ and protonation steps to generate H_2S.

Although the majority of hypoxia-activated prodrugs have been applied for cancer therapy, this type of activation can also be employed for other pathologies. In particular, reduction-activated approaches to deliver the gasotransmitters nitric oxide (NO) and hydrogen sulfide (H_2S), selectively in hypoxic conditions have found promise for managing different pathologies associated with this microenvironment.[20–24] Previously, our group has used metal complexes and metal-organic frameworks that release hydrogen sulfide (H_2S) for the treatment of hypoxic conditions including ischemia-reperfusion injury and dermal lesions.[25–27] Of particular significance was the complex

$[(H_2O)(NH_3)_4Ru(\mu\text{-}S_2)Ru(NH_3)_4(OH_2)]^{4+}$ (**[2]$^{4+}$**), originally reported by Taube and coworkers,[28,29] which we subsequently demonstrated to selectively release H_2S after chemical reduction.[27] The proposed mechanism for the reductive H_2S release from this complex requires a 4 e^- reduction of the [RuSSRu] fragment to break the S–S bond, yielding intermediate Ru^{2+} hydrosulfide complexes that liberate H_2S upon protonation (Scheme 1). The high redox potential of this compound makes its reduction by numerous biological reductants accessible, allowing it to be used for H_2S delivery under hypoxic conditions.

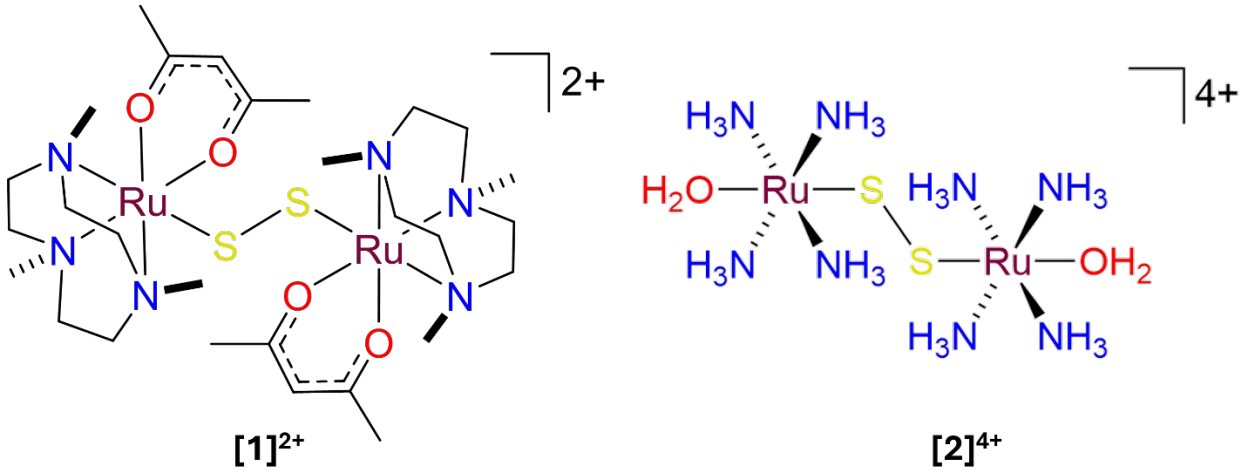

Chart 1. $[(Me_3TACN)(acac)Ru(\mu\text{-}S_2)Ru(acac)(Me_3TACN)]^{2+}$ (**[1]$^{2+}$**) and $[(H_2O)(NH_3)_4Ru(\mu\text{-}S_2)Ru(NH_3)_4(OH_2)]^{4+}$ (**[2]$^{4+}$**) studied in this work.

Given the value of **2** as a reduction-activated H_2S donor, a wide range of related persulfide-bridged dinuclear ruthenium complexes could also be considered for this application.[30–37] Among these different complexes, we chose to investigate the H_2S-release capability of the complex $[(Me_3TACN)(acac)Ru(\mu\text{-}S_2)Ru(acac)(Me_3TACN)]^{2+}$ (**[1]$^{2+}$**) where Me_3TACN = 1,4,7-trimethyl-1,4,7-triazacyclononane and acac = acetylacetonate (Chart 1). This complex was selected due to its reported high stability, which would make it valuable for aqueous biological applications.[33] Building on the prior characterization of **[1]$^{2+}$**, we sought to probe its ability to release H_2S under

reducing conditions. We found that **[1]**$^{2+}$ exhibits a remarkable stability to biological reductants, effectively failing to release H_2S under any relevant conditions. In addition to providing new characterization of **[1]**$^{2+}$, we also present density functional theory (DFT) calculations that provide a rationale for the resistance of **[1]**$^{2+}$ to reductive H_2S release compared to **[2]**$^{4+}$.

Results and Discussion

Synthesis and Characterization

Compound **[1]**$^{2+}$ was synthesized following the procedures in the literature and characterized using ^{1}H NMR, Raman, and UV-vis spectroscopies (Figures S1–S3, SI).[33,38] The ^{1}H NMR spectrum of this compound reveals it to be symmetric about the persulfide bridge with only a single set of resonances present for the acac and Me_3TACN ligands. Its UV-vis spectrum reveals an intense band centered at 799 nm that has previously been assigned to arise from the π_3–π_4 HOMO-LUMO transition within the π orbital manifold of the [RuSSRu] core (Figure 1).[34] Raman spectroscopy was also used to probe Ru–S and S–S stretching modes of **[1]**$^{2+}$. In a previous study of $[(H_3N)_5Ru(\mu\text{-}S_2)Ru(NH_3)_5]^{4+}$, the irradiation of an aqueous sample of this compound with a 647 nm laser resulted in a resonance Raman-enhanced peak at 415 cm^{-1}, which was assigned to the symmetric Ru–S stretch.[38] Irradiation with higher energy lasers (488, 531, and 568 nm) led to enhancement of the weaker symmetric S–S stretch at 519 cm^{-1}. In this study, we observed a similar phenomenon for **[1]**$^{2+}$ and **[2]**$^{4+}$, where excitation at 627 nm produces a strong resonance Raman effect and enhancement of the symmetric Ru–S stretching mode and excitation at 488 nm enhanced the peak from the symmetric S–S stretching mode. The symmetric Ru–S stretching modes were found at 418 and 409 cm^{-1}, while the corresponding S–S symmetric stretches were found at 530 and 497 cm^{-1} for **[1]**$^{2+}$ and **[2]**$^{4+}$, respectively (Figures S3–S4, SI). Related persulfide-bridged complexes

$[(PPh_3)_2(Cp)Ru(\mu\text{-}S_2)Ru(Cp)(PPh_3)_2]^{2+}$ where Cp = cyclopentadienyl and $[Cl(P(OMe)_3)_2Ru(\mu\text{-}S_2)(\mu\text{-}Cl)_2Ru(P(OMe)_3)_2Cl]$ have ν_{Ru-S} resonances at 408 and 385 cm^{-1}, respectively and ν_{S-S} resonances at 530 and 456 cm^{-1}, respectively.[31,36] The S–S stretching mode of **[1]**$^{2+}$ is higher in energy than those of **[2]**$^{4+}$ and these related complexes, reflecting a larger S–S force constant within **[1]**$^{2+}$.

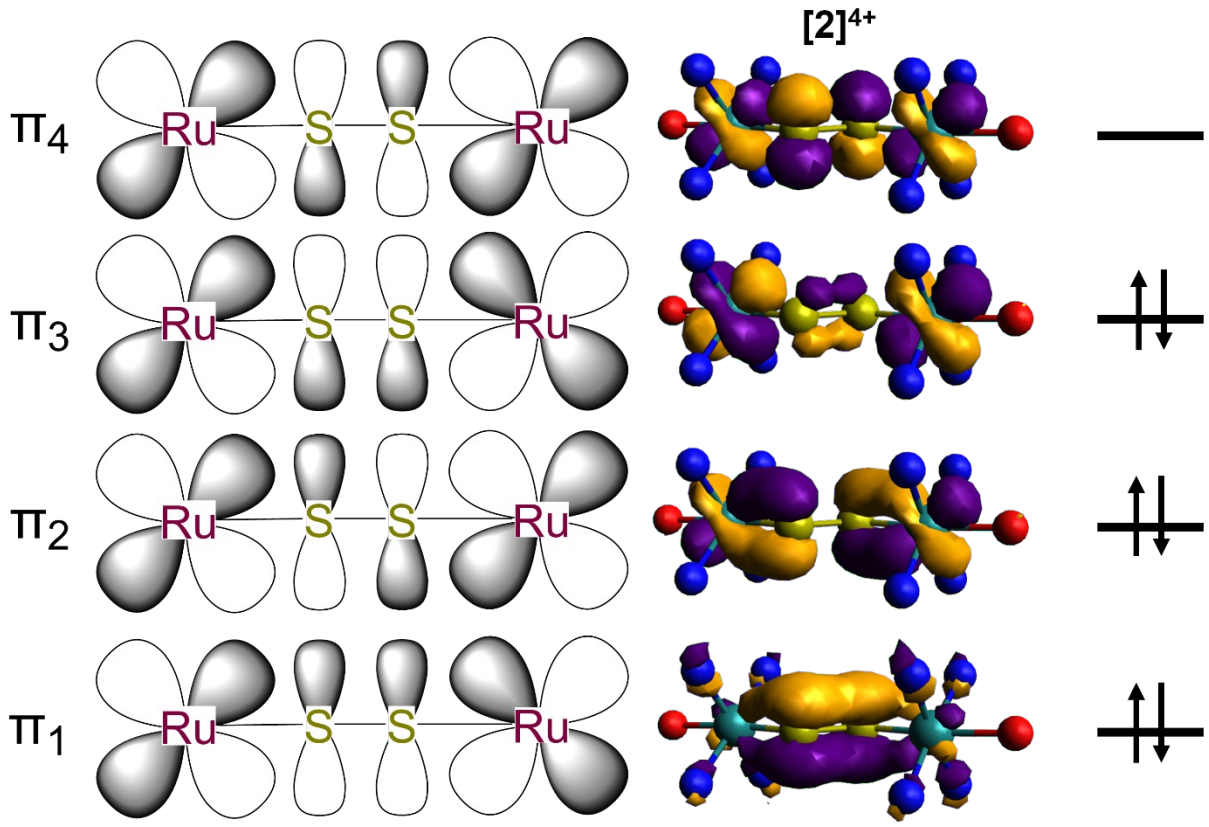

Figure 1. DFT-calculated Kohn-Sham orbitals representing the π system of [RuSSRu] in complex **[2]**$^{4+}$.

The crystal structure of **[1]**$^{2+}$ was previously determined, but with data collected at 298 K. Here, the crystal structure of **[1]**$^{2+}$ was redetermined from a data set obtained at 109 K. This reinvestigation identified crystals of **[1]**$^{2+}$ that attained a conformation distinct from the earlier study. Although both the new and old crystal structures belong to the $P\bar{1}$ space group, their unit cell parameters are significantly different, and our newly identified solvate co-crystallizes with a solvent

acetone molecule. Significantly, the conformations of $[\mathbf{1}]^{2+}$ within the two crystal structures are distinct. Within this newly reported structure, the acac and Me_3TACN ligands are arranged in a *syn* configuration ($[\mathbf{1\text{-}syn}]^{2+}$) about the [RuSSRu] core (Figure 2). By contrast, the earlier structure sits on a crystallographic inversion center, enforcing the acac and Me_3TACN ligands to be arranged in an *anti* configuration ($[\mathbf{1\text{-}anti}]^{2+}$). A comparison of the interatomic distances within these structures (Table 1) reveals that the S–S distance within $[\mathbf{1\text{-}syn}]^{2+}$ (2.0025 Å) is slightly longer than that in the earlier $[\mathbf{1\text{-}anti}]^{2+}$ (1.989 Å) (Table 1). This elongation may be due to the additional steric repulsion of the *syn* conformation, but effects due to temperature differences during data collection need also be considered. Despite distinct differences within these crystal structures, the ^{1}H NMR spectrum of this complex shows a single species in solution, suggesting that rotation about the S–S bond, to interconvert the *syn* and *anti* isomers, is rapid on the NMR timescale (Figure S1, SI).

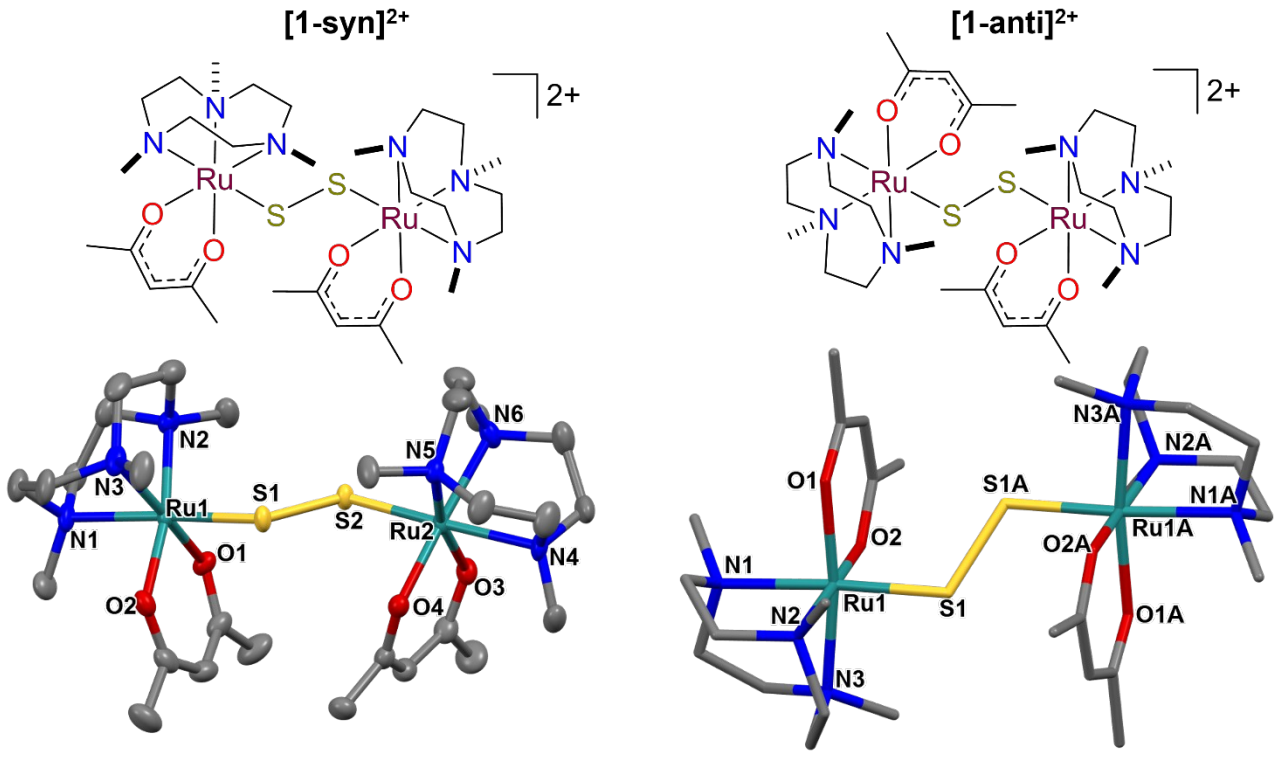

Figure 2. Crystal structure of **[1]**$^{2+}$, crystallized in *syn* (CCDC 2551495) and *anti* (CCDC 1232852) conformations. Counterions, hydrogen atoms, and solvent molecules are omitted for clarity. Thermal ellipsoids for **[1-syn]**$^{2+}$ are shown at a 50% probability level. **[1-anti]**$^{2+}$ is presented as a ball and stick model. Grey = C, red = O, blue = N, yellow = S, and teal = Ru. Crystallographic information for **[1-syn]**$^{2+}$ is given in Table S1, Supplementary Information.

Table 1. Selected interatomic distances (Å) in **1-syn** and **1-anti**.[a]

	[1-syn]$^{2+}$	**[1-anti]**$^{2+b}$
Ru_1–S_1	2.2156(7)	2.202(2)
Ru_1–N_1	2.177(2)	2.174(3)
Ru_1–N_2	2.127(3)	2.127(3)
Ru_1–N_3	2.126(3)	2.128(3)
Ru_1–O_1	2.034(2)	2.063(2)
Ru_1–O_2	2.045(2)	2.040(3)
Ru_2–S_2	2.2180(7)	
Ru_2–N_4	2.168(2)	
Ru_2–N_5	2.126(2)	
Ru_2–N_6	2.130(3)	
Ru_2–O_3	2.046(2)	
Ru_2–O_4	2.037(2)	
S_1–$S_{2/1A}$	2.0025(10)	1.989(2)

[a]Atoms are labeled as shown in Figure 2. Values in parentheses indicate the standard uncertainty in the last significant figure. [b]**[1-anti]**$^{2+}$ was reported previously in ref 33 and the structure collected at T = 298 K. Because this species sits on a crystallographic inversion center, only one set of interatomic distances are reported.

Stability to Chemical Reduction and Electrochemistry

In a previous report, reduction of **[2]**$^{4+}$ perturbed the $\pi_3 \rightarrow \pi_4$ transition within the [RuSSRu] core, a process that could be easily detected via the bleaching of the low-energy absorbance band at 700 nm using UV-Vis spectroscopy. Complex **[1]**$^{2+}$, likewise, possesses an analogous low-energy absorbance band at 799 nm, characteristic of the π–π^* transition within the [RuSSRu] moiety. In order to probe the propensity of the [RuSSRu] core within **[1]**$^{2+}$ to undergo reduction, a prerequisite for H_2S release from this class of compounds, solutions of this complex were treated with various biological reductants. A 20 μM solution of this complex was incubated in the presence of 1 mM of different biological reducing agents including cysteine, glutathione, and bisulfite, a strong reducing agent with a formal reduction potential ($E_0^{'}$) around –0.750 V vs the saturated calomel electrode (SCE).[39] Incubation of **[1]**$^{2+}$ with these reducing agents at pH 7.4 for 1 h at 37 °C resulted in minimal spectroscopic changes (Figure S6, SI). This result is in contrast to **[2]**$^{4+}$, which revealed a rapid decrease in this characteristic absorbance band over 1.5 h and concomitant release of H_2S under identical conditions, the degree of which correlated with the reducing strength of the reductant used. Therefore, **[1]**$^{2+}$ does not respond to these biological reductants like **[2]**$^{4+}$, reflecting a difference in either thermodynamics or kinetics of reduction.

In this context, both **[1]**$^{2+}$ and **[2]**$^{4+}$ were previously studied by cyclic voltammetry to assess their redox properties. The cyclic voltammogram of complex **[2]**$^{4+}$ was collected in phosphate-buffered saline (PBS) with a glassy carbon working electrode, whereas that of **[1]**$^{2+}$ was collected in acetonitrile with a glassy carbon working electrode. For complex **[2]**$^{4+}$, an important feature in the voltammogram is an irreversible reduction is observed with an onset potential of –716 mV vs SCE.

Prior voltammograms for **[1]**$^{2+}$ collected in acetonitrile, by contrast, show two quasi-reversible reductions centered at –974 and –1754 mV vs. SCE. These features were assigned to the [RuSSRu]$^{4+}$ to [RuSSRu]$^{3+}$ reduction and [RuSSRu]$^{3+}$ to [RuSSRu]$^{2+}$ reduction, respectively. Of key importance is that the reduction features of **[1]**$^{2+}$ are quasi-reversible, suggesting that this species can accommodate two additional electrons without cleavage of the S–S bond. When studied in pH 7.4 PBS, where the anti and syn conformers also rapidly interconvert, the voltammogram of **[1]**$^{2+}$ is appreciably different. Under these conditions, the only significant feature detected within the solvent window is an irreversible reduction with a peak potential at –758 mV vs SCE (Figure S7, SI). For comparison, the voltammogram of **[2]**$^{4+}$ characterized a previous transition to be centered around –716 mV. Given the more positive reduction potential of **[2]**$^{4+}$, this species should be more easily reduced than **[1]**$^{2+}$, which is consistent with our previously reported UV-vis data, where there were minimal changes to the spectroscopic profile of **[2]**$^{4+}$ under reducing conditions. Though this reductive wave within **[1]**$^{2+}$ occurs at more negative voltage which is consequential to its reduction, this potential falls within the electrochemical window of PBS and should be accessible by biological reducing agents. A computational approach was taken to elaborate upon the origins of these experimental findings.

DFT Calculations

The significantly greater stability of **[1]**$^{2+}$ compared to **[2]**$^{4+}$ towards biological reducing agents was investigated by density functional theory (DFT) calculations. The geometries of complexes **[1]**$^{2+}$ and **[2]**$^{4+}$ were optimized in the presence of an implicit solvation model and with an empirical dispersion correction to account for the effects of dissolution in water and weak intramolecular interactions, respectively. Coordinates from the crystal structures of these

complexes were used as the starting point for these geometry optimizations. As noted above, the two crystal structures of $[\mathbf{1}]^{2+}$ reveal different orientations of the supporting acac and Me_3TACN ligands, giving the *syn* and *anti* conformations. The *syn* conformation was found to be 1.60 kcal/mol higher in energy than the *anti* conformer. Because these conformers are very close in energy and most likely interconvert in solution, our subsequent DFT calculations were carried out with both conformers. From the frequency calculations of the ground state singlet, the symmetric S–S stretching frequencies for $\mathbf{[1\text{-}anti]^{2+}}$, $\mathbf{[1\text{-}syn]^{2+}}$, and $\mathbf{[2]^{4+}}$ were calculated to be 552.21, 561.66, and 538.51 cm^{-1}, respectively. The calculated values for S–S stretches are in good agreement with the experimental Raman data, where $\mathbf{[1\text{-}syn]^{2+}}$ and $\mathbf{[1\text{-}anti]^{2+}}$ have higher energy stretching frequencies compared to $\mathbf{[2]^{4+}}$, suggestive of a larger bond order.

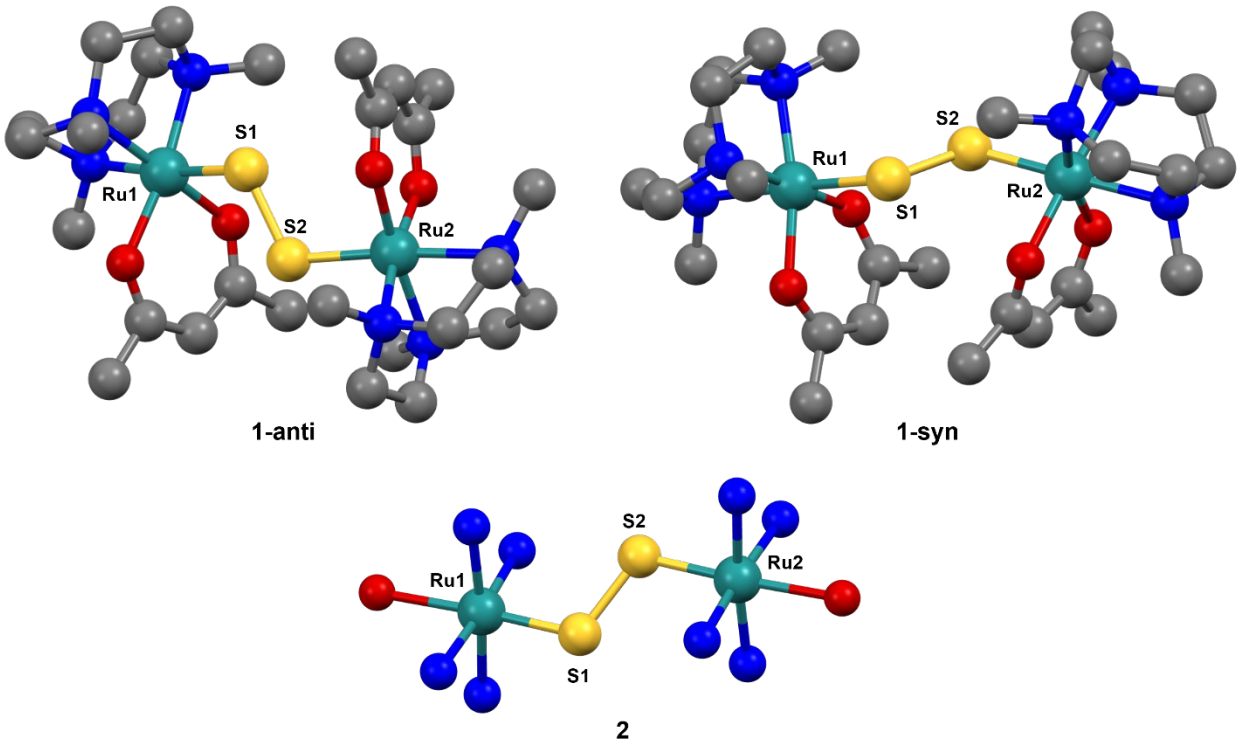

Figure *3*. DFT-optimized structures of the two conformers of **[1]**$^{2+}$, **[1-anti]**$^{2+}$ and **[1-syn]**$^{2+}$, and **[2]**$^{4+}$ with numbering schemes consistent to those presented in Figure 2. Interatomic distances are shown in Table 2.

Figure 4 shows the Kohn-Sham molecular orbitals (MOs) and their respective energies for **[1-anti]**$^{2+}$, **[1-syn]**$^{2+}$, and **[2]**$^{4+}$. The relative orbital energies and topologies are similar to those qualitatively discussed in a prior study for complexes containing the [RuSSRu] core (Figure 1). Consistent with this earlier MO description, the highest occupied molecular orbital (HOMO) for all of these species is characterized by its S–S π-bonding and Ru–S π* antibonding nature, whereas the lowest unoccupied molecular orbital (LUMO) is a π* antibonding orbital with nodes between each of the four atoms.[34] The HOMO-LUMO gaps of **[1-syn]**$^{2+}$, **[1-anti]**$^{2+}$**,** and **[2]**$^{4+}$ are 1.744, 1.915, and 1.913 eV, respectively. The calculated gaps for **[1-syn]**$^{2+}$, **[1-anti]**$^{2+}$**,** and **[2]**$^{4+}$ correspond to λ values of 710 nm, 647 nm and 648 nm, which are consistent with the experimentally observed transitions centered at 799 and 700 nm, respectively.

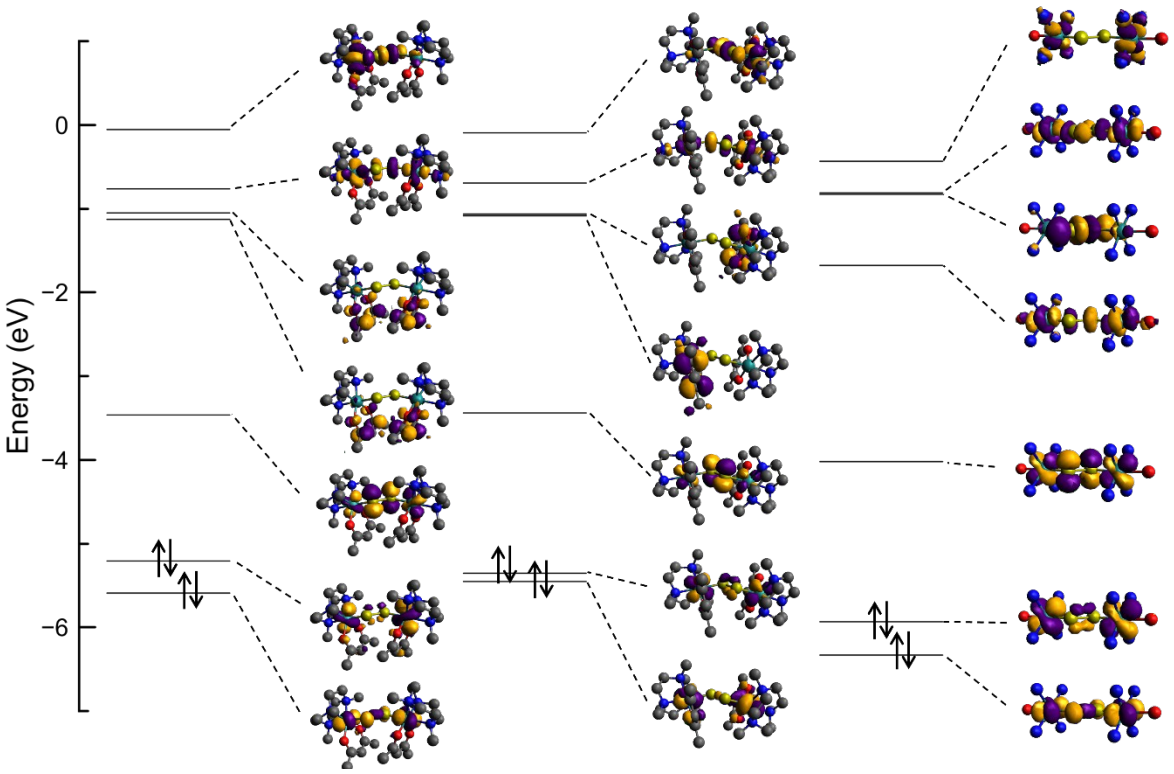

Figure 4. Kohn-Sham MO diagram for **[1-syn]**$^{2+}$ (left), **[1-anti]**$^{2+}$ (middle), and **[2]**$^{4+}$ (right) plotted at iso values of 0.04.

As proposed previously, complex **[2]**$^{4+}$ requires 4e$^-$ and 4 H$^+$ to cleave the persulfide bridge, releasing two equivalents of H_2S and two Ru^{2+}complexes. The 4e$^-$ are needed to populate the two S–S π^* and σ^* antibonding orbitals to achieve full cleavage of the persulfide bond. As noted above, for all three complexes the LUMO is the π_4 MO, and therefore their 2e$^-$ reduction should destabilize the S–S bond. For **[2]**$^{4+}$, the LUMO+1 is S–S σ^* in nature, and further reduction of this complex should lead to clean S–S bond cleavage. By contrast, the analogous S–S σ^* MO in both **[1-syn]**$^{2+}$ and **[1-anti]**$^{2+}$ is the LUMO+4, and consequently it is expected that the other intervening acac-based orbitals would need to be populated before S–S bond cleavage can be accessed.

To computationally investigate these reduction steps, the geometries of the complexes were optimized after introducing additional electrons to the models. The addition of 2 e$^-$ resulted in

significantly altered structures. In all the complexes, the HOMO of the double reduced species becomes the RuSSRu π^* antibonding orbital, which was previously the LUMO in starting complexes (Figure 5). For complex **[2]$^{2+}$**, the LUMO of the 2 e$^-$-reduced product can be described as an S–S σ^* MO, the population of which is required to cleave the S–S bond. By contrast, the corresponding S–S σ^* MOs of **[1-syn]** and **[1-anti]** remain several levels above the LUMO.

A decrease in S–S and Ru–S bond orders upon the 2 e$^-$-reduction of these complexes was apparent in an analysis of their interatomic distances (Table 2). The interatomic distances of Ru_1–S_1, Ru_2–S_2, and S_1–S_2 within **[1-syn]**, **[1-anti]**, and **[2]$^{2+}$** all exhibited a pronounced increase within the 2 e$^-$-reduced structures. The Ru–S and S–S interatomic distances increased by 0.17–0.19 Å and 0.13–0.15 Å, respectively, due to filling of S–S π^* orbitals of all species. Complex **2** exhibited an increase in the S–S bond distance of 0.15 Å, larger than the 0.13 Å elongation observed for **[1-anti]** and **[1-syn]**. This reduction also led to geometric changes in the Ru–S–S–Ru torsion angles, presumably due to loss of the double bond character of the S–S interaction which would otherwise force planarity (Figures S8–S10, SI). The torsion angle decreased from 180.00° to 99.95° in complex **[2]$^{2+}$** . Complex **[1-anti]$^{2+}$** experienced a similar decrease from 154.08° to 99.56°. For **[1-syn]$^{2+}$**, from the torsion angle decreased to a lesser degree, changing from 158.83° to 127.52°. This result may be a consequence of the steric restrictions enforced by Me_3TACN and acac ligands with the *syn* arrangement. The torsion angles present in **[1-syn]$^{2+}$** and **[1-anti]$^{2+}$** of 158.83° and 154.08° are both much smaller than that of **[2]$^{4+}$**, reflecting the greater steric congestion introduced by the bulky Me_3TACN and acac ligands.

Table 2. Selected Interatomic Distances for **[1-syn]$^{2+}$**, **[1-anti]$^{2+}$**, and **[2]$^{4+}$**, and their 2e$^-$ and 4e$^-$-Reduced Analogues as Calculated with DFT[a]

	1-syn			**1-anti**			**2**		
Reduced Species	**[1-syn]$^{2+}$**	**[1-syn]**	**[1-syn]$^{2-}$**[b]	**[1-anti]$^{2+}$**	**[1-anti]**	**[1-anti]$^{2-}$**[b]	**[2]$^{4+}$**	**[2]$^{2+}$**	**[2]**
Ru_1–S_1 (Å)	2.278	2.469	2.496	2.267	2.466	2.483	2.216	2.389	2.459
Ru_2–S_2 (Å)	2.274	2.474	2.492	2.266	2.473	2.490	2.216	2.388	2.458
S_1–S_2 (Å)	2.020	2.155	2.173	2.010	2.153	2.175	2.031	2.184	5.036

[a]Atoms are labeled as shown in Figure 3. [b]Structures were optimized as the ground state triplet.

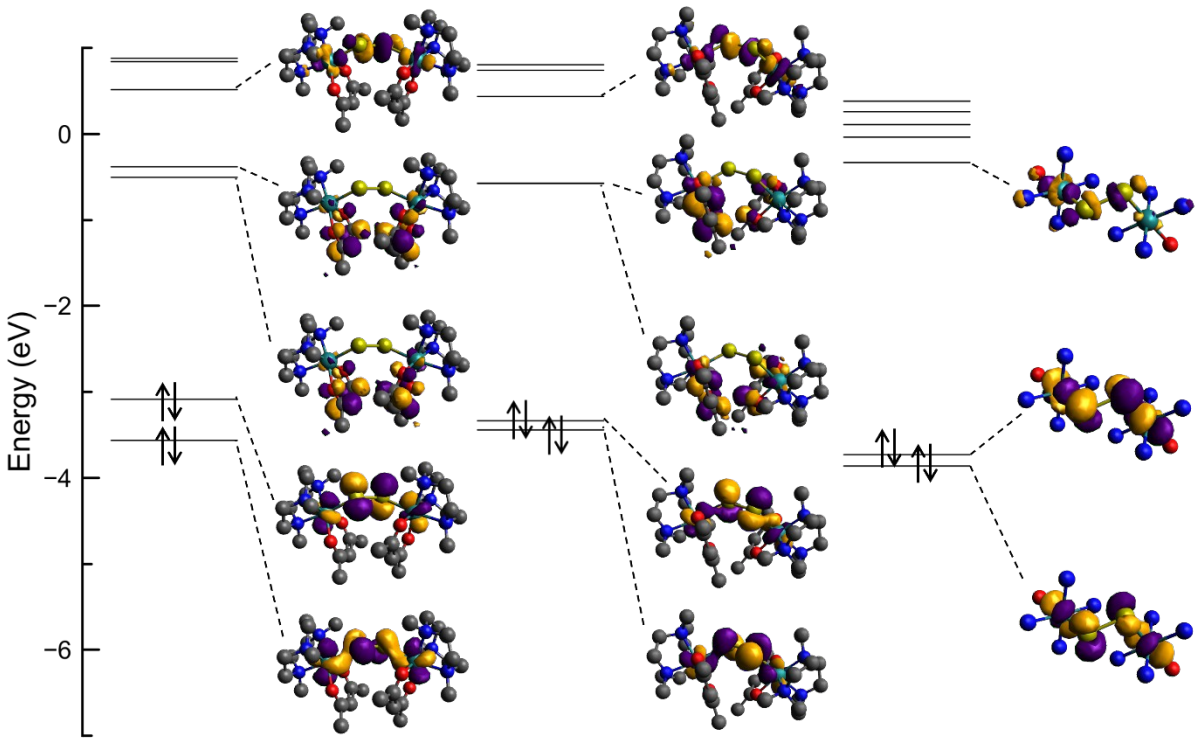

Figure 5. Kohn-Sham MO diagram of the 2 e^--reduced **[1-syn]** (left), **[1-anti]** (middle), and **[2]**$^{2+}$ (right), plotted at iso value of 0.04.

This reduction process was further modeled by optimizing the structures after the addition of two more e^-. In contrast to the 4 e^--reduced **[2]**, the 4 e^--reduced forms, **[1-anti]**$^{2-}$ and **[1-syn]**$^{2-}$ were more stable in the triplet state, owing to the degeneracy of the HOMO and HOMO–1 orbitals. The triplet states for these species were 11.2 and 19.6 kcal·mol^{-1} lower in energy than the corresponding singlet states. With the triplet state being identified as a lower energy state than the singlet, we also considered the possibility for antiferromagnetic or ferromagnetic coupling. For the antiferromagnetic coupled triplet, the energies of **[1-syn]**$^{2-}$ and **[1-anti]**$^{2-}$ were only 0.055 and 0.002 kcal·mol^{-1} higher in energy than the open shell triplet, effectively indistinguishable within the error for DFT calculations. Likewise, the ferromagnetically coupled triplet state for **[1-syn]**$^{2-}$ and **[1-anti]**$^{2-}$ was also indistinguishable from the open shell triplet with respective energies of 0.0004

and 0.013 kcal·mol^{-1}. Thus, this 4 e$^-$-reduced species is probably best described as a simple paramagnet with S = 3. This result is expected because the spin density of the triplet state shows that unpaired electrons to reside within orbitals on the acac ligands on opposite sides of the complex. The large spatial separation of the electron spins would not lead to any expected strong antiferromagnetic or ferromagnetic coupling. With the addition of these two extra electrons, major structural and electronic differences between complexes **[1]**$^{2-}$ and **[2]** are apparent. As shown in Table 3, there is a significant increase in the S–S interatomic distance within **[2]**, in the 4 e$^-$-reduced form, increasing from 2.184 to 5.036 Å, indicating complete cleavage of this bond to afford two discrete Ru^{2+} complexes. By contrast, there are only slight changes in the S–S interatomic distances within **[1-syn]**$^{2-}$ and **[1-anti]**$^{2-}$ where the values increased from 2.155 to 2.173 Å and 2.153 to 2.175 Å, respectively. These small changes can be attributed to the fact that the HOMOs within the 4 e$^-$-reduced species are π^* orbitals of the acac ligands, which do not directly affect the S–S bond orders (Figure 6). Likewise, the Ru–S distances elongated a negligible amount, changing from 2.469 to 2.496 Å and 2.474 to 2.492 Å for **[1-syn]**$^{2-}$, and 2.466 to 2.483 Å and 2.473 to 2.490 Å for **[1-anti]**$^{2-}$. These results suggests that a 4 e$^-$ reduction is sufficient for the cleavage of the S–S bond in **[2]**$^{4+}$, but not for **[1]**$^{2+}$, since electrons are placed within unrelated acac π^* orbitals, which do not affect S–S interactions. Based on the MO diagram, full cleavage of the S–S bond within **1** would require injection of an additional 4 e$^-$ to populate the S–S σ^* orbitals (Figure 6). These results starkly contrast with **[2]**, where S–S σ^* orbitals were populated to cause cleavage of the S–S bond and generate two identical complexes.

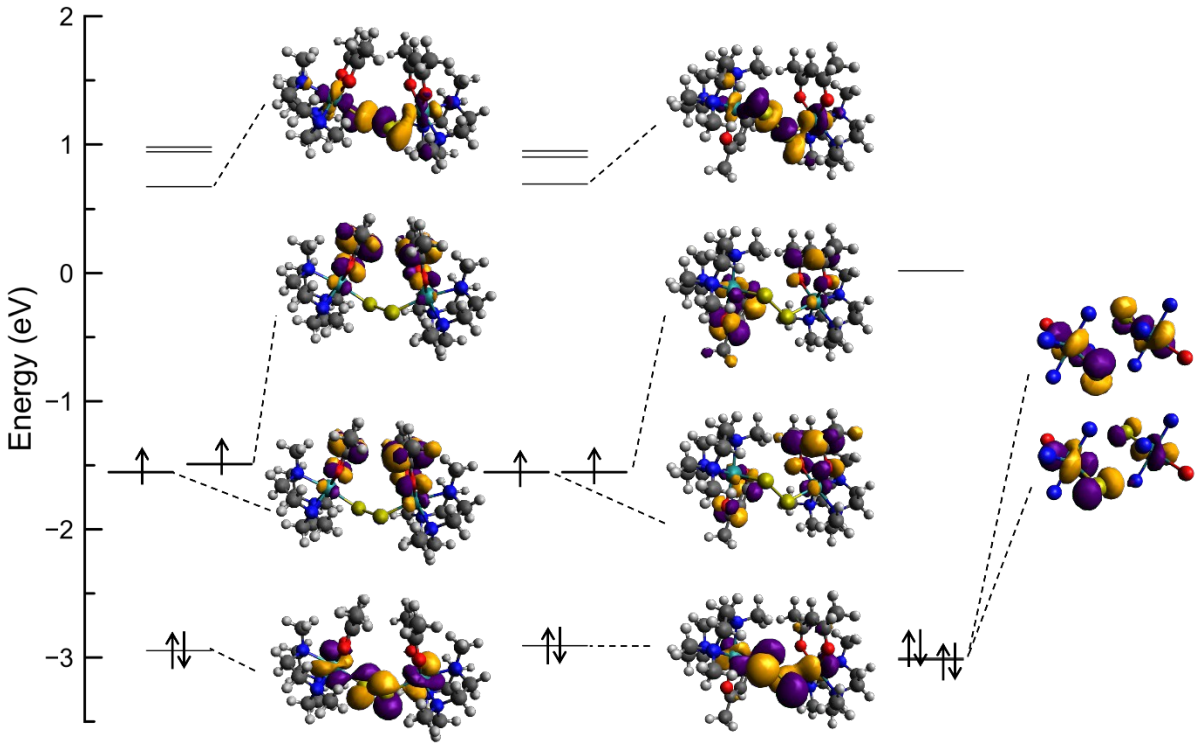

Figure 6. Kohn-Sham MO diagram of the 4 e^--reduced **[1-syn]**$^{2-}$ (left), **[1-anti]**$^{2-}$ (middle), and **[2]** (right) plotted at iso value of 0.04. Both **[1-syn]**$^{2-}$ and **[1-anti]**$^{2-}$ were optimized in the triplet state, whereas **[2]** was optimized as a singlet.

These DFT calculations suggest that intermediary acac π* orbitals possibly prevent the reductive cleavage of the [RuSSRu] moiety. To quantify the favorability of these reduction processes, the adiabatic two- and four-electron affinities of the complexes were calculated using the difference between the reduced and unreduced species (Table 3). Larger values indicate a more stable product formed as a result of reduction, indicating a greater favorability for the process. When the 2 e^- reduction was modeled, we calculated the electron affinity to be 6.60, 6.57, and 7.97 eV for the formation of **[1-syn]**, **[1-anti]**, and **[2]**, respectively, suggesting the thermodynamic favorability of the 2 e^-reduction of **[2]**$^{4+}$. Subsequent reduction by 2 e^-, however, shows a significant difference in the electron affinity with values found to be 2.21, 2.22, and 4.92 eV, respectively. The dramatic decrease in the adiabatic electron affinity of **[1-syn]** and **[1-anti]** suggests that population

of the acac π* orbitals is less favorable comparatively to the population of S–S π* orbital as seen in **[2]**$^{2+}$. Collectively, these DFT results can explain the lack of reactivity of **[1]**$^{2+}$ with biological reductants compared to **[2]**$^{4+}$, as well as the . The low-lying π* orbitals of the acac ligand can accommodate additional electrons, whereas these additional electron with **[2]**$^{2+}$ are deposited within the S–S σ* MO. Furthermore, the electron affinities of **[1]**$^{2+}$ get progressively smaller as additional electrons are added, presumably due to charge accumulation that additionally decreases the favorability for multi-electron reduction.

Table 3. Computed Adiabatic Electron Affinities (eV) for **1-syn**, **1-anti**, and **2**.

	0 → 2 e$^-$	**2 e$^-$ → 4e$^-$**	**0 → 4 e$^-$**	**EA′**
1-syn	6.60	2.21	8.82	16.13 [a]
1-anti	6.57	2.22	8.79	16.03 [b]
2	7.97	4.92	12.89	16.96 [c]

[a] EA′ was calculated for the process **[1-syn]**$^{2+}$ + $2H_3O$ → 2[Ru(Me_3TACN)(acac)(SH)] + $2H_2O$. [b] EA′ was calculated for the process **[1-anti]**$^{2+}$ + $2H_3O$ → 2[Ru(Me_3TACN)(acac)(SH)] + $2H_2O$. [c] EA′ was calculated for the process **[2]**$^{4+}$ + $2H_3O$ → 2[Ru(NH_3)$_4$(OH_2)(SH)] + $2H_2O$.

The preceding calculations suggest that intermediary acac π* orbitals possibly prevent the reductive cleavage of the [RuSSRu] moiety. A significant limitation of this model is the omission of protons, a choice made to circumvent a principal limitation of DFT, which is an inability to calculate proton energies and easily consider proton concentrations within the context of an optimization. The electron affinity calculations above do not consider the importance of protons in facilitating both electron capture and cleavage of the S–S bond. To probe the role of protons, we calculated electron affinities (EA′) for the proton-coupled processes shown in Eqs 1 and 2, which lead to formation of the mononuclear hydrosulfide complexes. The EA′ value for **[2]**$^{4+}$ is more favorable by 0.82 and 0.89 eV compared to either **[1-syn]**$^{2+}$ or **[1-anti]**$^{2+}$, respectively. Thus, this result mirrors the simpler calculations of the adiabatic electron affinities, suggesting that

protonation does not significantly change the comparative favorability of reduction of these complexes. We caution the sole utilization of these results to draw conclusions on the reactivity of the system, but instead suggest consideration of these calculations within the context of thorough molecular orbital analyses and experimental results.

$$1+4e^{-}+2H_3O^{+}\rightarrow 2\left[Ru(Me_3TACN)(acac)(SH)\right]+2H_2O \quad (1)$$

$$2+4e^{-}+2H_3O^{+}\rightarrow 2\left[Ru(NH_3)_4(OH_2)(SH)\right]^{n+}+2H_2O \quad (2)$$

Conclusion

Our experimental investigation of complex **[1]**$^{2+}$ revealed it to be impervious towards reduction by biological reducing agents. Consequently, the [RuSSRu] motif of this complex remained intact, as verified by its characteristic absorbance at 799 nm, and failed to release H_2S, marking a significant contrast to the behavior of the previously studied complex **[2]**$^{4+}$. The electrochemistry of these complexes in aqueous solution reveals a slightly more positive reduction potential for **[2]**$^{4+}$ compared to **[1]**$^{2+}$, which contributes to the more facile reduction of **[2]**$^{4+}$. DFT analysis of the electronic structures of these compounds suggests important differences that contribute to their varying behavior in the presence of reducing agents. The divergence of chemical behavior and the reduction potential can be attributed to differences in the electronic structure of these two ions. We ascribe the absence of H_2S release within **[1]**$^{2+}$ specifically to the availability of unoccupied acac π^* orbitals that can accommodate electrons more readily than the S–S σ^* orbital, the population of which is essential to the cleavage of the S–S bond and subsequent release of the therapeutic gas. By comparison, the S–S σ^* orbital within **[2]**$^{4+}$ was found to be more accessible due to the absence of intervening π^* orbitals. Although this property precludes the use of **[1]**$^{2+}$ as an

H_2S-releasing agent, it may be useful for other applications, such as for photocatalytic H_2 production.[30] These results have important implications on the design of future dinuclear persulfide-bridged H_2S donors, suggesting that supporting ligands with low-lying unoccupied orbitals should be avoided.

Experimental Details

Reagents and Materials

All reagents were obtained commercially and used without further purification. Complex **[1]**$^{2+}$ was prepared as previously described and characterized via NMR spectroscopy, Raman spectroscopy, UV-vis spectroscopy, and elemental analysis according to literature procedures.[33]

Physical Measurements

1D-NMR (^{1}H) spectra were acquired at 25 °C on a 500 MHz Bruker AV 3HD spectrometer equipped with a broadband Prodigy cryoprobe (Bruker, Billerica, MA). UV-vis spectra were recorded using 1 cm quartz cuvettes and a Shimadzu UV-1900 spectrometer (Shimadzu, Kyoto, Japan) fitted with a temperature-controlled circulating water bath. Elemental analyses (C,H,N) were carried out by Atlantic Microlab Inc. (Norcross, GA).Raman spectra were collected on solid samples using a Horiba Jobin Yvon T64000 open-frame confocal microscope with triple monochromator and LN2-cooled CCD detector. An Olympus MPlan 50× objective was used to focus the incident beam. Signals were calibrated against a silicon standard before each measurement. Excitation sources included a mixed gas Ar/Kr ion laser at 488, 514, and 647 nm. The power of the incident beams was set to 115 μW, 120 μW, and 115 μW, respectively. .

Spectroscopic Characterization

Compound **[1]**$^{2+}$ was prepared as a PF_6 salt using literature procedures and was purified by vapor diffusion of ether into an acetone solution. ^{1}H NMR (500 MHz, DMSO) δ (ppm) = 5.45 (s, 2H), 3.66–3.58 (m, 4H), 3.31 (d, *J* = 8.1 Hz, 9H), 3.02–2.95 (m, 4H), 2.89–2.82 (m, 5H), 2.64 (d, *J* = 8.0 Hz, 4H), 2.55 (s, 12H), 2.36 (s, 6H), 1.92 (s 12H). Elemental analysis (C,H,N): calc'd (% for $C_{28}H_{56}F_{12}N_6O_4P_2Ru_2S_2$) C 30.66; H 5.15; N 7.66. Found (%) C 30.30; H 5.08; 7.53. Raman (488 nm) ν (cm^{-1}) = 189 (w), 213 (vw), 284 (vw), 317 (vw), 357(w), 421 (m), 459 (m), 531 (m), 684 (w), 742 (w), 769 (w), 789 (w), 840 (vw).

X-Ray Crystallography

Single crystals of **[1]**$^{2+}$ were obtained by vapor diffusion of hexanes into an acetone solution of the complex. Low-temperature X-ray diffraction data for 1 were collected on a Rigaku XtaLAB Synergy diffractometer coupled to a Rigaku Hypix detector with Mo Kα radiation (λ = 0.71073 Å, from PhotonJet micro-focus X-ray sources at 100 K. The diffraction images were processed and scaled using the CrysAlisPro software (Rigaku Oxford Diffraction, The Woodlands TX). The structures were solved through intrinsic phasing using SHELXT[40] and refined against F^2 on all data by full matrix least squares with SHELXL[41] following established refinement strategies.[42] All nonhydrogen atoms were refined anisotropically. All hydrogen atoms bound to carbon were included in the model at geometrically calculated positions and refined using a riding model. Details of the data quality and a summary of the residual values of the refinements are listed in Table S1. Acetone was present within the crystal. The acetone molecule, along with one PF_6 counterion showed positional disorder. These disorders were modeled using appropriate distance and thermal displacement restraints, while allowing the occupancies of the disordered components to freely refine to a sum of unity. CCDC 2551495 contains the supplementary crystallographic data

for this paper. These data can be obtained free of charge via www.ccdc.cam.ac.uk/data_request/cif, or by emailing data_request@ccdc.cam.ac.uk, or by contacting The Cambridge Crystallographic Data Centre, 12 Union Road, Cambridge, CB2 1EZ, UK; fax: +44 1223 336033

Thermal Stability

The thermal stability of the complex was assessed using ^{1}H NMR and UV-Vis spectroscopies. Samples were incubated at 37 ºC for both studies. UV-Vis studies were performed in 1× PBS. A 20 μM sample of **[1]**$^{2+}$ was prepared in buffer and monitored every 60 min for 18 h. NMR spectra were acquired in DMSO-d_6 at a concentration of 10 mM collected every 24 h for 72 h.

Treatment with Reducing Agents

The stability of the complex to reducing agents cysteine, glutathione, and sodium bisulfite was determined using UV-vis spectroscopy. A 20 mM sample of **[1]**$^{2+}$ was prepared in 1× PBS (pH 7.4, 37 °C) and coincubated with 1 mM of each reducing agent. The UV-vis spectrum was monitored every 60 min for 8 h.

Electrochemical Measurement

Electrochemical measurements were carried out using a Pine Wavedriver 10 potentiostat with a three-electrode setup consisting of a glassy carbon working electrode, a platinum counter electrode, and an Ag/AgCl quasi-reference electrode. All potentials were referenced to the $[Ru(NH_3)_6]^{3+/2+}$ redox couple at –0.193 V vs saturated calomel electrode (SCE) as an internal standard.[43] The sample cell was deoxygenated by bubbling nitrogen gas through the solution for 5 min prior to analysis and maintained under a blanket of nitrogen during the experiment.

Computational Studies

DFT calculations were performed using Gaussian 16.[44] All calculations were carried out using the hybrid B3LYP functional.[45,46] The LANL2DZ basis set and effective core potential were used for ruthenium atoms, and the 6-31G(d,p) basis set was used for the other elements.[47] Geometry optimizations were performed in a self-consistent reaction field (SCRF) using an SMD model to simulate the solvation of the compounds in water while also accounting for empirical dispersion using the D3 version of Grimme's dispersion.[48] Starting geometries of the complexes were modeled after their crystal structures.[27,33] After geometry optimization, frequency calculations were carried out to ensure that the geometries had converged to local minima on the potential energy surface. The Cartesian coordinates of all optimized structures are provided as part of the Supporting Information. Molecular orbitals were visualized and rendered at an isovalue of 0.04 using Avogadro 1.2.0.

Calculation of antiferromagnetic states was performed following the Gaussian tutorial (gaussian.com/afc/). Starting energies were calculated using the triplet state structure optimization and frequency calculation for the 4 e^--reduced species, **[1-syn]$^{2-}$** and **[1-anti]$^{2-}$**. A stability check was performed on the wavefunction of this species using kewords "geom=check" and "stable=opt". After the wavefunction was determined to be stable, the molecule was parsed into fragments for a fragment guess job. For **[1]$^{2-}$**, we separated the ion into three fragments. Fragment 1 and 2 encompassed each one acac ligand. This selection was made due to the presence of spin density in these corresponding orbitals. Fragment 3 awas comprised of the [RuSSRu] core and the supporting Me_3TACN ligands. Fragments 1 and 2 were characterized as having a doublet spin multiplicity with –1 charge on each and were defined as "alpha" and "beta" spin multiplicities, respectively. Fragment 3 was defined as having "alpha" sin multiplicity. After the fragment guess job completes,

a stability calculation was rerun on the output to verify wavefunction stability. The result should present an output where the Mulliken atomic spin densities are approximately equal and of opposite signage. Ferromagnetic states were calculated analogously, however, in the fragment guess job all fragments were defined as having “alpha” spin density.

Thermodynamics Calculations

Default settings in Gaussian16 yield free energies under standard state conditions in the gas phase (1 atm, 298 K). To adjust these values for standard state solution conditions (1 M concentration for solute or pure liquid state for solvent), a correction to the gas-phase free energy terms was applied. For solutes, the correction factor in moving from 1 atm (or 1/24.5 M) follows the following expression:

$$RTln\left(\frac{1\,M}{1\,atm}\right)=RTln(24.5)=7.9\,kJ\bullet mol^{-1}$$

For H_3O^+, the free energy was adjusted to account for the concentration of this species under buffered conditions

$$RTln\left(\frac{3.16\times10^{-8}}{1\,atm}\right)=RTln(7.74\times10^{-7})=-34.9\,kJ\bullet mol^{-1}$$

Acknowledgements

This research was supported by Cornell University, the University of California Santa Barbara, and the National Science Foundation (NSF) of the United States of America under award number CHE-

2203369. This work made use of the Cornell NMR facility, which is supported in part by the NSF (CHE-1531632).

Conflicts of Interest

The authors declare no conflict of interest.

Associated Content

Supporting Information

The Supporting Information is available free of charge at

- Supplementary data for chemical synthesis, Raman spectroscopy, X-ray crystallographic tables, NMR spectroscopy, cyclic voltammograms, UV-vis and NMR thermal stability, and torsion angle measurements (PDF)
- XYZ coordinates of computed structures (ZIP)
- Crystallographic data including .cif files and IUCr CheckCIF for **1** (CIF)

Accession Code

CCDC 2551495 contains the supplementary crystallographic data for this paper. These data can be obtained free of charge via www.ccdc.cam.ac.uk/data_request/cif, or by emailing data_request@ccdc.cam.ac.uk, or by contacting The Cambridge Crystallographic Data Centre, 12 Union Road, Cambridge CB2 1EZ, UK; fax: +44 1223 336033.

Author Information

Corresponding Author

Justin J. Wilson – *Department of Chemistry and Biochemistry, University of California, Santa Barbara, California 93106, United States; Department of Chemistry and Chemical Biology, Cornell University, Ithaca, New York 14853, United States;* orcid.org/0000-0002-4086-7982; Email: justinjwilson@ucsb.edu

Author

Piyusha S. Lotlikar – *Department of Chemistry and Chemical Biology, Cornell University, Ithaca, New York 14853, United States; Department of Chemistry and Biochemistry, University of California, Santa Barbara, California 93106, United States;* orcid.org/0000-0002-0458-9655

References

(1) Lefere, S.; Van Steenkiste, C.; Verhelst, X.; Van Vlierberghe, H.; Devisscher, L.; Geerts, A. Hypoxia-Regulated Mechanisms in the Pathogenesis of Obesity and Non-Alcoholic Fatty Liver Disease. *Cell. Mol. Life Sci.* **2016**, *73*, 3419–3431. https://doi.org/10.1007/s00018-016-2222-1.

(2) Rosmorduc, O.; Housset, C. Hypoxia: A Link between Fibrogenesis, Angiogenesis, and Carcinogenesis in Liver Disease. *Semin. Liver Dis.* **2010**, *30*, 258–270. https://doi.org/10.1055/s-0030-1255355.

(3) Heyman, S. N.; Khamaisi, M.; Rosen, S.; Rosenberger, C. Renal Parenchymal Hypoxia, Hypoxia Response and the Progression of Chronic Kidney Disease. *Am. J. Nephrol.* **2008**, *28*, 998–1006. https://doi.org/10.1159/000146075.

(4) Della Rocca, Y.; Fonticoli, L.; Rajan, T. S.; Trubiani, O.; Caputi, S.; Diomede, F.; Pizzicannella, J.; Marconi, G. D. Hypoxia: Molecular Pathophysiological Mechanisms in Human Diseases. *J. Physiol. Biochem.* **2022**, *78*, 739–752. https://doi.org/10.1007/s13105-022-00912-6.

(5) Merelli, A.; Repetto, M.; Lazarowski, A.; Auzmendi, J. Hypoxia, Oxidative Stress, and Inflammation: Three Faces of Neurodegenerative Diseases. *J. Alzheimers Dis.* **2021**, *82* , S109–S126. https://doi.org/10.3233/JAD-201074.

(6) Nath, B.; Szabo, G. Hypoxia and Hypoxia Inducible Factors: Diverse Roles in Liver Diseases. *Hepatology* **2012**, *55*, 622–633. https://doi.org/10.1002/hep.25497.

(7) Tumor Hypoxia in Cancer Therapy. In *Methods in Enzymology*; Academic Press, 2007; pp 295–321. https://doi.org/10.1016/S0076-6879(07)35015-5.

(8) Brown, J. M.; Wilson, W. R. Exploiting Tumour Hypoxia in Cancer Treatment. *Nat. Rev. Cancer* **2004**, *4*, 437–447. https://doi.org/10.1038/nrc1367.

(9) Eltzschig, H. K.; Bratton, D. L.; Colgan, S. P. Targeting Hypoxia Signalling for the Treatment of Ischaemic and Inflammatory Diseases. *Nat. Rev. Drug. Discov.* **2014**, *13*, 852–869. https://doi.org/10.1038/nrd4422.
(10) Sharma, A.; Arambula, J. F.; Koo, S.; Kumar, R.; Singh, H.; Sessler, J. L.; Kim, J. S. Hypoxia-Targeted Drug Delivery. *Chem. Soc. Rev.* **2019**, *48*, 771–813. https://doi.org/10.1039/C8CS00304A.
(11) Wilson, W. R.; Hay, M. P. Targeting Hypoxia in Cancer Therapy. *Nat. Rev. Cancer* **2011**, *11*, 393–410. https://doi.org/10.1038/nrc3064.
(12) Li, Y.; Zhao, L.; Li, X.-F. Targeting Hypoxia: Hypoxia-Activated Prodrugs in Cancer Therapy. *Front. Oncol.* **2021**, *11,* 700407. https://doi.org/10.3389/fonc.2021.700407.
(13) Nagasawa, H.; Uto, Y.; Kirk, K. L.; Hori, H. Design of Hypoxia-Targeting Drugs as New Cancer Chemotherapeutics. *Biol. Pharmacol. Bull.* **2006**, *29*, 2335–2342. https://doi.org/10.1248/bpb.29.2335.
(14) Zeng, Y.; Ma, J.; Zhan, Y.; Xu, X.; Zeng, Q.; Liang, J.; Chen, X. Hypoxia-Activated Prodrugs and Redox-Responsive Nanocarriers. *Int. J. Nanomed.* **2018**, *13*, 6551–6574. https://doi.org/10.2147/IJN.S173431.
(15) Kobus, M.; Friedrich, T.; Zorn, E.; Burmeister, N.; Maison, W. Medicinal Chemistry of Drugs with N-Oxide Functionalities. *J. Med. Chem.* **2024**, *67*, 5168–5184. https://doi.org/10.1021/acs.jmedchem.4c00254.
(16) Chen, Y.; Hu, L. Design of Anticancer Prodrugs for Reductive Activation. *Med. Res. Rev.* **2009**, *29*, 29–64. https://doi.org/10.1002/med.20137.
(17) Brown, J. M.; Wilson, W. R. Exploiting Tumour Hypoxia in Cancer Treatment. *Nat. Rev. Cancer* **2004**, *4*, 437–447. https://doi.org/10.1038/nrc1367.
(18) Graf, N.; Lippard, S. J. Redox Activation of Metal-Based Prodrugs as a Strategy for Drug Delivery. *Adv. Drug Deliv. Rev.* **2012**, *64*, 993–1004. https://doi.org/10.1016/j.addr.2012.01.007.
(19) Phillips, A. M. F.; Pombeiro, A. J. L. Transition Metal-Based Prodrugs for Anticancer Drug Delivery. *Curr. Med. Chem.* **2019**, *26*, 7476–7519. https://doi.org/10.2174/0929867326666181203141122.
(20) Li, X.; Cai, J.; Zhang, H.; Sun, S.; Zhao, S.; Wang, Z.; Nie, X.; Xu, C.; Zhang, Y.; Xiao, H. A Trisulfide Bond Containing Biodegradable Polymer Delivering Pt(IV) Prodrugs to Deplete Glutathione and Donate H_2S to Boost Chemotherapy and Antitumor Immunity. *ACS Nano* **2024**, *18*, 7852–7867. https://doi.org/10.1021/acsnano.3c06194.
(21) Zhou, W.; Ma, C.; Wang, Y.; Yang, W.; Gou, S. Hypoxia-Activated Dual Donors of H_2S and NO Alleviate Myocardial Injury in Coronary Heart Disease *via* Synergistic Mechanisms. *Eur. J. Med. Chem.* **2026**, *307*, 118671. https://doi.org/10.1016/j.ejmech.2026.118671.
(22) Bag, S.; Ghosh, D.; Seth, A.; De, P. Nitroreductase (NTR)-Triggered Degradable Polymeric Sulfur Dioxide (SO_2) Prodrug. *Biomacromolecules* **2025**, *26*, 7540–7552. https://doi.org/10.1021/acs.biomac.5c01047.
(23) Zhang, N.; Li, T.; Zhong, P.; Fu, T.; Li, L.; Peng, M.; Wang, Y.; Lu, Y.; Yao, M. Design and Synthesis of a NTR-Sensitive Fluorescent H2S Donor as a Potential Therapeutic Agent for Myocardial Ischemia–Reperfusion Injury. *J. Med. Chem.* **2025**, *68*, 14981–14994. https://doi.org/10.1021/acs.jmedchem.5c01169.
(24) Xu, X.; Sun, M.; Luo, X.; Zhang, Z.; Su, L.; Cui, L.; Zhu, Z.; Lu, X.; Wang, R.; Han, F.; Qian, X.; Yang, Y. One-Electron Reduction Triggered Nitric Oxide Release for Ischemia-

Reperfusion Protection. *Free Radic. Biol. Med.* **2021**, *164*, 13–19. https://doi.org/10.1016/j.freeradbiomed.2020.12.443.
(25) Woods, J. J.; Cao, J.; Lippert, A. R.; Wilson, J. J. Characterization and Biological Activity of a Hydrogen Sulfide-Releasing Red Light-Activated Ruthenium(II) Complex. *J. Am. Chem. Soc.* **2018**, *140*, 12383–12387. https://doi.org/10.1021/jacs.8b08695.
(26) Chen, F. E.; Mandel, R. M.; Woods, J. J.; Lee, J.-H.; Kim, J.; Hsu, J. H.; Fuentes-Rivera, J. J.; Wilson, J. J.; Milner, P. J. Biocompatible Metal–Organic Frameworks for the Storage and Therapeutic Delivery of Hydrogen Sulfide. *Chem. Sci.* **2021**, *12*, 7848–7857. https://doi.org/10.1039/D1SC00691F.
(27) Woods, J. J.; Wilson, J. J. A Dinuclear Persulfide-Bridged Ruthenium Compound Is a Hypoxia-Selective Hydrogen Sulfide (H_2S) Donor. *Angew. Chem. Int. Ed.* **2021**, *60*, 1588–1592. https://doi.org/10.1002/anie.202012620.
(28) Brulet, C. R.; Isied, S. S.; Taube, H. Disulfur Binuclear Ruthenium Ammines. *Journal of the American Chemical Society* **1973**, *95*, 4758–4759. https://doi.org/10.1021/JA00795A051/ASSET/JA00795A051.FP.PNG_V03.
(29) Stein, C. A.; Taube, H. Ruthenium Ammine Disulfides. *Inorg. Chem.* **1979**, *18*, 2212–2216. https://doi.org/10.1021/ic50198a033.
(30) Gao, Y.; Qian, B.-F.; Wang, J.-L.; Jia, A.-Q.; Mei, Q.; Zhang, Q.-F. *μ*-Disulfido Complexes of Ruthenium(III) 1,1′-Dithiolate $[(Me_3Tacn)Ru_2(\kappa^2\text{-}S_2COR)(\kappa^2\text{-}S_2C{=}O)(\mu\text{-}S_2)]PF_6$ (Me_3Tacn = 1,4,7-Trimethyl-1,4,7-Triazacyclononane; R = Alkyl). *Inorg. Chim. Acta.* **2023**, *548*, 121374. https://doi.org/10.1016/j.ica.2022.121374.
(31) Amarasekera, J.; Rauchfuss, T. B.; Wilson, S. R. Synthesis, Structure, and Properties of $[CpRu(PR_3)_2]_2(\mu\text{-}S_2)^{2+}$. Effects of Strong π-Donation in a Disulfur Complex. *Inorg. Chem.* **1987**, *26*, 3328–3332. https://doi.org/10.1021/ic00267a023
(32) Chatterjee, D.; Chrzanowska, M.; Katafias, A.; Oszajca, M.; Van Eldik, R. Ru^{III}(Edta) Complexes as Molecular Redox Catalysts in Chemical and Electrochemical Reduction of Dioxygen and Hydrogen Peroxide: Inner-Sphere *versus* Outer-Sphere Mechanism. *RSC Adv.* **2021**, *11*, 21359–21366. https://doi.org/10.1039/d1ra03293c.
(33) Schneider, R.; Wieghardt, K.; Nuber, B. New μ-Disulfido and μ-Diselenido Complexes of Ruthenium(III). Crystal Structure of $[LRu^{III}(Acac)_2(\mu\text{-}S_2)](PF_6)_2$ (L = 1,4,7-Trimethyl-1,4,7-Triazacyclononane; Acac = Pentane-2,4-Dionate). *Inorg. Chem.* **1993**, *32*, 4935–4939. https://doi.org/10.1021/ic00074a045
(34) Sellmann, D.; Lechner, P.; Knoch, F.; Moll, M. Transition-Metal Complexes with Sulfur Ligands. 82.[1] H_2S, S_2, and CS_2 Molecules as Ligands in Sulfur-Rich $[Ru(PPh_3)'S_4']$ Complexes [('S_4')2- = 1,2-Bis[(2-Mercaptophenyl)Thio]Ethane(2-)). *J. Am. Chem. Soc.* **1992**, *114*, 922–930. https://doi.org/10.1021/ja00029a020
(35) Sellmann, D.; Barth, I. Transition Metal Complexes with Sulfur Ligands XLVII. S_2 Bridged Ruthenium Complexes with Sulfur Dominated Coordination Spheres and Highly Unusual Electronic Properties: $[\mu\text{-}S_2\{Ru(PPh_3)('S_4')\}_2]$ and $[\mu\text{-}S_2\{Ru(PPh_3)('^{bu}S_4')\}2]$ ('S_4'$^{2-}$ = 1,2-Bis(2-Mercaptophenylthio)Ethane (2—); '$^{bu}S_4$'$^{2-}$ = 1,2-Bis(3,5-Di(Tertiarybutyl)-2-Mercaptophenylthio)Ethane (2—)). *Inorg. Chim. Acta.* **1989**, *164*, 171–177. https://doi.org/10.1016/S0020-1693(00)83219-3.
(36) Matsumoto, K.; Matsumoto, T.; Kawano, M.; Ohnuki, H.; Shichi, Y.; Nishide, T.; Sato, T. Syntheses and Crystal Structures of Disulfide-Bridged Binuclear Ruthenium Compounds: The First UV-Vis, Raman, ESR, and XPS Spectroscopic Characterization of a Valence-

Averaged Mixed-Valent $Ru^{III}SSRu^{II}$ Core. *J. Am. Chem. Soc.* **1996**, *118*, 3597-3609. https://doi.org/10.1021/ja950391v

(37) Sun, T.-T.; Gao, Y.; Chen, C.; Jia, A.-Q.; Zhang, Q.-F. *μ*-Disulfido Ruthenium(III) Complexes with [(Me_3Tacn)Ru] Units Stabilized by Dialkyl-1,1′-Dithiophosphate Ligands (Me_3Tacn = 1,4,7-Trimethyl-1,4,7-Triazacyclononane). *J. Mol. Struct.* **2025**, *1345*, 143109. https://doi.org/10.1016/j.molstruc.2025.143109.

(38) Kim, Soonhee; Otterbein, Elizabeth S.; Rava, Richard P.; Stephan S. Isied; Joseph San Filippo, Jr.; Joseph V. Waszcyak. Resonance Raman Spectra and Electronic Structure of the μ-Disulfur-Bridged Diruthenium Complex $[(H_3N)_5RuSSRu(NH_3)_5]^{4+}$ and Related Systems. *J. Am. Chem. Soc.* **1983**, *105*, 336–339. https://doi.org/10.1021/ja00341a006

(39) Michal, G.; Schomburg, D. *Biochemical Pathways: An Atlas of Biochemistry and Molecular Biology*; John Wiley & Sons, Ltd, 2012. https://doi.org/10.1002/9781118657072.

(40) Sheldrick, G. M. A Short History of SHELX. *Acta Cryst A* **2008**, *64*, 112–122. https://doi.org/10.1107/S0108767307043930.

(41) Sheldrick, G. M. Crystal Structure Refinement with SHELXL. *Acta Cryst C* **2015**, *71*, 3–8. https://doi.org/10.1107/S2053229614024218.

(42) Müller, P. Practical Suggestions for Better Crystal Structures. *Crystallography Rev.* **2009**, *15*, 57–83. https://doi.org/10.1080/08893110802547240.

(43) Lim, H. S.; Barclay, D. J.; Anson, F. C. Formal Potentials and Cyclic Voltammetry of Some Ruthenium-Ammine Complexes. *Inorg. Chem.* **1972**, *11*, 1460–1466. https://doi.org/10.1021/ic50113a003.

(44) M. J. Frisch and G. W. Trucks and H. B. Schlegel and G. E. Scuseria and M. A. Robb and J. R. Cheeseman and G. Scalmani and V. Barone and G. A. Petersson and H. Nakatsuji and X. Li and M. Caricato and A. V. Marenich and J. Bloino and B. G. Janesko and R. Gomperts and B. Mennucci and H. P. Hratchian and J. V. Ortiz and A. F. Izmaylov and J. L. Sonnenberg and D. Williams-Young and F. Ding and F. Lipparini and F. Egidi and J. Goings and B. Peng and A. Petrone and T. Henderson and D. Ranasinghe and V. G. Zakrzewski and J. Gao and N. Rega and G. Zheng and W. Liang and M. Hada and M. Ehara and K. Toyota and R. Fukuda and J. Hasegawa and M. Ishida and T. Nakajima and Y. Honda and O. Kitao and H. Nakai and T. Vreven and K. Throssell and Montgomery, {Jr.}, J. A. and J. E. Peralta and F. Ogliaro and M. J. Bearpark and J. J. Heyd and E. N. Brothers and K. N. Kudin and V. N. Staroverov and T. A. Keith and R. Kobayashi and J. Normand and K. Raghavachari and A. P. Rendell and J. C. Burant and S. S. Iyengar and J. Tomasi and M. Cossi and J. M. Millam and M. Klene and C. Adamo and R. Cammi and J. W. Ochterski and R. L. Martin and K. Morokuma and O. Farkas and J. B. Foresman and D. J. Fox. Gaussian 16, Revision C.01, 2016.

(45) Becke, A. D. Density-functional Thermochemistry. III. The Role of Exact Exchange. *J. Chem. Phys.* **1993**, *98*, 5648–5652. https://doi.org/10.1063/1.464913.

(46) Lee, C.; Yang, W.; Parr, R. G. Development of the Colle-Salvetti Correlation-Energy Formula into a Functional of the Electron Density. *Phys. Rev. B* **1988**, *37*, 785–789. https://doi.org/10.1103/PhysRevB.37.785.

(47) Hay, P. J.; Wadt, W. R. Ab Initio Effective Core Potentials for Molecular Calculations. Potentials for K to Au Including the Outermost Core Orbitals. *The Journal of Chemical Physics* **1985**, *82*, 299–310. https://doi.org/10.1063/1.448975.

(48) Marenich, A. V.; Cramer, C. J.; Truhlar, D. G. Universal Solvation Model Based on Solute Electron Density and on a Continuum Model of the Solvent Defined by the Bulk Dielectric

Constant and Atomic Surface Tensions. *J. Phys. Chem. B* **2009**, *113*, 6378–6396. https://doi.org/10.1021/jp810292n.

For Table of Contents Only: